Modal Analysis of β-Ga_2O_3:Cr Widely Tunable Luminescent Optical Microcavities

M. Alonso-Orts,[1] E. Nogales,[1,*] J. M. San Juan,[2] M. L. Nó,[3] J. Piqueras,[1] and B. Méndez[1]

[1]*Departamento de Física de Materiales, Facultad de Ciencias Físicas, Universidad Complutense de Madrid, 28040 Madrid, Spain*

[2]*Departamento de Física de la Materia Condensada, Facultad de Ciencias y Tecnología, Universidad del País Vasco, Apdo. 644, 48080 Bilbao, Spain*

[3]*Departamento de Física Aplicada II, Facultad de Ciencia y Tecnología, Universidad del País Vasco, Apdo. 644, 48080 Bilbao, Spain*

(Received 27 November 2017; revised manuscript received 20 March 2018; published 7 June 2018; corrected 9 August 2018)

Optical microcavities are key elements in many photonic devices, and those based on distributed Bragg reflectors (DBRs) enhance dramatically the end reflectivity, allowing for higher quality factors and finesse values. Besides, they allow for wide wavelength tunability, needed for nano- and microscale light sources to be used as photonic building blocks in the micro- and nanoscale. Understanding the complete behavior of light within the cavity is essential to obtaining an optimized design of properties and optical tunability. In this work, focused ion-beam fabrication of high refractive-index contrast DBR-based optical cavities within Ga_2O_3:Cr microwires grown and doped by the vapor-solid mechanism is reported. Room-temperature microphotoluminescence spectra show strong modulations from about 650 nm up to beyond 800 nm due to the microcavity resonance modes. Selectivity of the peak wavelength is achieved for two different cavities, demonstrating the tunability of this kind of optical system. Analysis of the confined modes is carried out by an analytical approximation and by finite-difference–time-domain simulations. A good agreement is obtained between the reflectivity values of the DBRs calculated from the experimental resonance spectra, and those obtained by finite-difference–time-domain simulations. Experimental reflectivities up to 70% are observed in the studied wavelength range and cavities, and simulations demonstrate that reflectivities up to about 90% could be reached. Therefore, Ga_2O_3:Cr high-reflectivity optical microcavities are shown as good candidates for single-material-based, widely tunable light emitters for micro- and nanodevices.

DOI: 10.1103/PhysRevApplied.9.064004

I. INTRODUCTION

Optical microcavities are key elements in many photonic devices. They can be fabricated with photonic crystals, Fabry-Perot, or distributed-Bragg-reflector (DBR) cavities [1], whispering gallery modes [2,3], or wave-guided modes [4]. Some of their functionalities are biosensors [3,5], optical filters, lasers [1], quantum memory [6], or energy harvesting [7]. Since the first fabrication of a photonic-band-gap microcavity within a silicon waveguide by x-ray lithography [8], the idea is extended to micro- and nanowires, creating the periodic pattern by techniques such as electron-beam lithography [9–11] or focused-ion-beam (FIB) milling [6,12,13]. Optical cavities based on DBRs enhance dramatically the end reflectivity, and allow for higher quality factors and finesse values. In this way, the patterned structure would serve at the same time as emitter, gain medium, and resonator. FIB deep etching allows the fabrication of a high-refractive-index contrast DBR, resulting in much shorter device lengths [9] than with two dielectric materials with low-refractive-index contrast [14] or than shallower FIB patterns [12,13]. On the other hand, recent work on microcavities is based many times on single-mode nanowires [1]. However, multimode fibers present very interesting characteristics for sensors [15] or supercontinuum lasers [16].

Among the different materials susceptible to be used as DBR-based microcavities, monoclinic β-Ga_2O_3 is of high interest. It is a transparent conductive oxide (TCO) that has attracted strong interest due to its high chemical and thermal stability, wide transparency range ($E_g \approx 4.9$ eV) [17], controllable conductivity [18], excellent properties for high-power electronics due to its very high breakdown field [19,20] as well as its biocompatibility [21,22].

Nano- and microscale light sources allowing for wavelength tunability are needed as photonic building blocks in the micro- and nanoscale, such as light-emitting devices, light detectors, or active optical switches [23]. Among the different materials susceptible to be used for this purpose, β-Ga_2O_3:Cr micro- and nanowires are of high interest due to several reasons. First of all, homogeneous broadening of the bands is needed for optical tunability from a single material [24] and Ga_2O_3:Cr fulfills this requisite due to its $^4T_2$–$^4A_2$, Cr^{3+} very intense luminescence transition. In

*enogales@ucm.es

several materials, tunability is obtained via compositional variations, including different dopants and/or alloys [1], while systems in which a wide tunability is obtained with no need of compositional variations, just by changing the cavity dimensions in the micro- and nanoscale, are scarce, e.g., CdS [25]. Besides, β-Ga_2O_3:Cr presents long decay times, in the range of 100 μs [26], which favors population inversion in order to be used as gain media. In fact, Cr^{3+} doped oxides are extensively used since the first laser, made of ruby (Al_2O_3:Cr) and later this ion is used for tunable lasers made of oxides such as chromium-doped alexandrite or emerald. Furthermore, Ga_2O_3 is the TCO with the widest band gap, which results in the widest transparency range among these materials, down to deep UV (≈250 nm). In fact, there are other intense broadbands, as well as sharp lines, emitted from doped and undoped Ga_2O_3 [27–29] that might be tuned from deep UV to the infrared thanks to these kinds of DBR-based microcavities. We show in this report that such tuning and effective confinement of light can be performed in this material through the reported photonic design.

This work merges luminescence of this material, micro- and nanowires, and photonic high-reflectivity microcavities. In particular, high-power electronics and controllable doping are expected to allow high luminescence yield to be achieved by electroluminescence in Ga_2O_3, which is the process currently used in many luminescent micro- and nanodevices. Electroluminescence is reported for Ga_2O_3 [30–32]. This high luminescence power will facilitate certain features, such as reaching population inversion. Micro- and nanodevices based on Ga_2O_3 will be of great interest for nanotechnology and they will benefit from the findings on Ga_2O_3 high-power applications [33,34]. Indeed, in the last years, consideration of semiconducting TCOs has changed from being traditionally considered as transparent electrodes with conductivity, to develop as an important area of semiconductor physics, photonics, and optoelectronics [35–38].

Undoped Ga_2O_3 presents a characteristic broad emission band in the UV-blue range due to intrinsic defects and/or dopants typically found in this material [27,28,39,40] beside the strong and tunable luminescence bands from the UV to the infrared via suitable doping [27–32]. In our previous works, we showed and completely characterized the strong emission band related to Cr^{3+} as a dopant of Ga_2O_3 [26], and the waveguiding behavior of the Ga_2O_3 micro- and nanowires doped with Cr and rare earths [41,42], but no optical modes were observed in those cases. Chromium-related luminescence at room temperature shows both the two sharp R lines due to the ^2E–$^4A_2$ intraionic transition and the broadband due to the $^4T_2$–$^4A_2$ transition. The latter is due to the phonon-related homogeneous broadening of the luminescence [24], resulting in a potential wide tunability of the luminescence of this material in the red-NIR range [26]. This fact opens up to potential applications of Cr-doped Ga_2O_3 to be used as a tunable optical gain medium. The anisotropy of monoclinic gallium-oxide crystal lattice leads to the spontaneous growth of microwires by thermal evaporation methods with an optimal aspect ratio for effective light waveguiding. Furthermore, we have previously reported the formation of more-complex morphologies, such as branches or crossed wires, by codoping Ga_2O_3 with Sn and Cr [43–45]. On the other hand, the high crystal quality and smooth lateral-wall surface of Ga_2O_3:Cr microwires enables some light confinement and we demonstrate Fabry-Perot resonances due to the reflection in their two ends, because of the refractive-index change between the material and the air [42]. However, reflectivity losses are the main drawback for these wires to be used as optical resonators, resulting in an acceptable quality factor but low finesse values. Since the NIR luminescence band is emitted by a long lifetime dopant ($\tau \sim 200$ μs–2 ms) [26], it would be desirable to achieve long photon lifetimes within the cavity, i.e., to improve Q and F. In the present work, we aim to get a significant advance on the control and performance of the optical cavities based on Ga_2O_3:Cr through the creation of DBRs.

Understanding the complete behavior of light within the cavity is essential in order to obtain good properties and allow both optimized design and use of the optical tunability. Homogeneous broadening of the red–near-infrared (NIR) luminescence band in Ga_2O_3:Cr allows experimental measurements and a thorough analysis of the cavity modes and discussion on further improvements by means of analytical models and numerical, finite-difference–time-domain–(FDTD) based simulations. High-reflectivity microcavities have not been explored so far in this material and we show their great potential, setting out a proof-of-principle design for single-material-based, widely tunable emitters for micro- and nanodevices with capabilities beyond the available optical range for a single material. For that aim, we have merged the previously acquired thorough physical knowledge on the optical emission properties of Ga_2O_3:Cr^{3+} [26,46], as well as the know-how to obtain self-formed microwires with desired dimensions and shapes, with the design, implementation, and optimization of DBR-based optical microcavities by means of analytical physical models and numerical simulations.

In this work, we report the FIB fabrication of high refractive-index contrast DBR-based optical cavities within Ga_2O_3:Cr microwires grown and doped in a single thermal step by the vapor-solid mechanism. Resonant modes are detected by polarized microphotoluminescence measurements and data are analyzed under both theoretical models of modal analysis in rectangular optical cavities and FDTD simulations. The results show that the patterned fibers exhibit an enhanced performance of the cavity light confinement with respect to the as-grown wires within a rather wide tunability range.

II. EXPERIMENTAL DETAILS

Ga_2O_3:Cr microwires doped during growth are fabricated in a single-step thermal treatment [42]. Cr cation atomic concentration is in the range of 0.5 at. %, as measured by EDX. Some of them are deposited on a TEM grid so that they are suspended in air, except for the carbon "mesh." DBR patterns are milled by FIB in a FEI Helios 650 at 30 kV and 24 pA for the ion column, in order to optimize the sharpness of the milled features and minimize the potential gallium contamination, as analyzed in previous milling works [47]. The design of the dimensions of each hole from the DBR, is made by FDTD simulations performed with OptiFDTD software. Ga_2O_3 has to be considered a dispersive medium in the wavelength range of interest because $(\omega/n)(dn/d\omega)$ is around 0.1 for the current frequencies. Therefore, the Sellmeier dispersion relation $\varepsilon = A + [B\lambda^2/(\lambda^2 - C^2)]$ is used, with parameters $A = 2.31$, $B = 1.14$, and $C = 0.24$ obtained from fitting the Sellmeier expression to experimental data from Al-Kuhaili *et al.* [48]. Morphology and actual dimensions of the FIB pattern analysis before and after patterning is performed either with a FEI Inspect or a JEOL JSM 7600F SEM. Electron-backscattered-diffraction (EBSD) analysis is performed with the FEI SEM, using the Bruker QUANTAX CrystAlign EBSD software. Room-temperature μ-PL spectra are acquired in a Horiba Jobin-Yvon LabRam 800 system with $\lambda_{exc} =$ 325 nm of a Kimmon HeCd laser.

III. RESULTS AND DISCUSSION

Figure 1(a) shows the SEM images of two optical cavities fabricated in a Ga_2O_3:Cr microwaveguide. Each cavity is created by drilling two sets of N rectangular holes, separated by a distance L, as shown schematically in Fig. 1(b). $N = 20$ and the unpatterned region has a length of $L_1 = 15.2$ μm in cavity 1. $N = 10$ and $L_2 = 15$ μm in cavity 2. Figure 1(c) shows a detail of the drills done into the waveguide. They completely cross the thickness of the wire and have a width $\alpha = 210$ nm and a length $\gamma = 570$ nm. The total period of the DBR is $\Lambda =$ 520 nm. The transversal dimension is $a = 1.15$ μm. Figure 1(d) shows a detail of the waveguide tilted 57°. From this image, we obtain the value of the thickness $b = 510$ nm. Besides, an edge is observed along this lateral side, indicating that the cross section is not rectangular. The actual cross-section shape is sketched in Fig. 1(e). To determine the upper surface plane of the microwire, EBSD analysis is performed. Kikuchi patterns obtained on the surface plane, Fig. 1(f), can be ascribed to monoclinic β-Ga_2O_3. The convoluted pole figure associated with Kikuchi patterns, inset in Fig. 1(f), allows identification of the surface plane to be (100).

Microphotoluminescence (μ-PL) analysis from the unpatterned microwire as well as from the two cavities is performed in the confocal microscope. Luminescence spectra are detected locally from one end of the structure of interest. On the other hand, the excitation with the laser

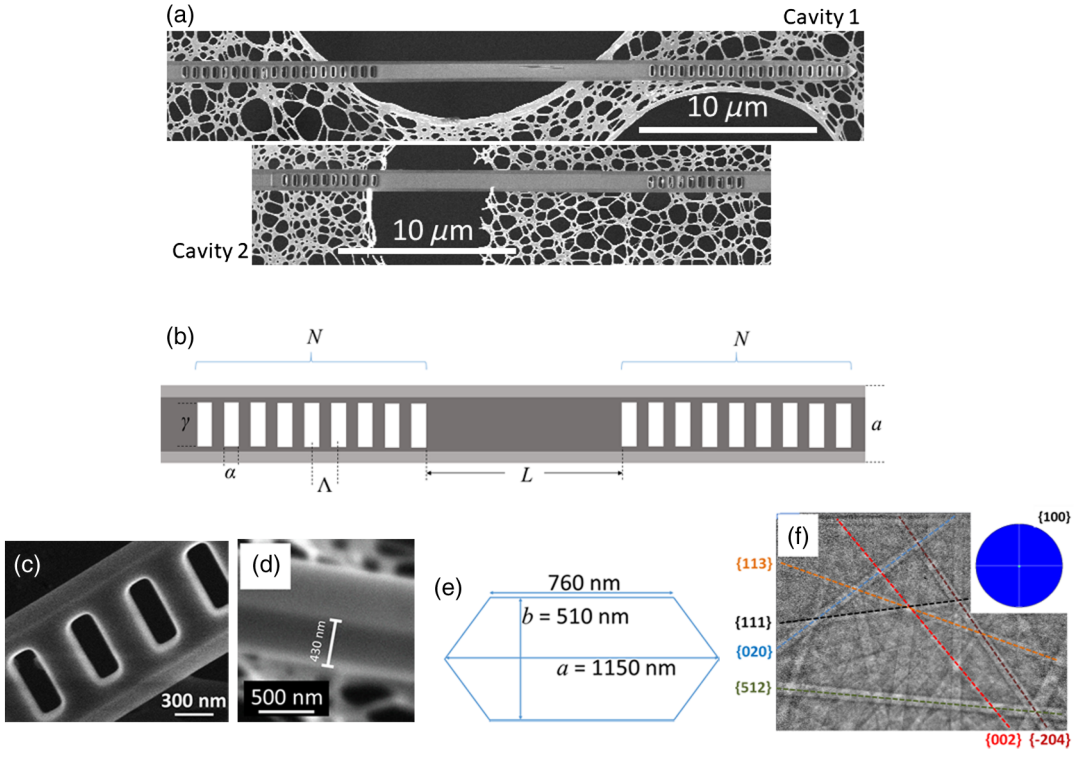

FIG. 1. (a) Top view SEM images of two optical cavities patterned on a waveguide. (b) Schematic of the different cavity parameters. (c) Top view detail of the wire and FIB drilled holes at 0° and (d) 57° tilt. (e) Sketch of the cross section of the wire. (f) EBSD pattern of the surface plane. The inset shows the convoluted pole figure of the surface plane for the [100] zone axis.

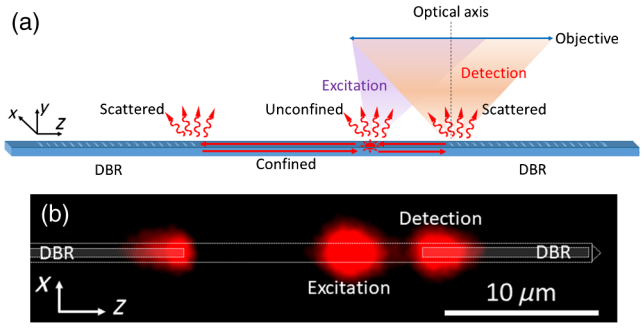

FIG. 2. (a) Schematic of the excitation-detection configuration in the μ-PL confocal system. (b) μ-PL image of cavity 1 indicating the excitation and detection points. White dotted lines represent the waveguide and the patterned DBRs, shown in Fig. 1(a).

($\lambda_{exc} = 325$ nm) is performed on a different point, as explained elsewhere [42,49]. This point is within the wire in the spectra from unpatterned wire and within the optical cavity in the spectra from the two FIB patterned cavities, as sketched in Fig. 2(a). Axes are defined in Fig. 2(a): x is perpendicular to both the microwire longitudinal axis and the optical axis of the system, z is parallel to the waveguide longitudinal axis (propagation direction), and y is parallel to the optical axis of the system. Figure 2(b) shows the room-temperature μ-PL image of cavity 1, shown in Fig. 1(a). White dotted lines indicate the wire and DBR positions, for the sake of clarity. Scattering of light is shown to occur essentially in the cavity end and DBR beginning.

Room-temperature μ-PL spectra from the unpatterned waveguide and cavities 1 and 2 are shown in Fig. 3(a). Spectrum from the unpatterned wire presents the characteristic $Ga_2O_3:Cr^{3+}$ luminescence, with two sharp R lines (691 and 698 nm) and the broadband due to the ^2E–$^4A_2$ and the $^4T_2$–$^4A_2$ intraionic transitions, respectively [26]. The inset shows a weak modulation of the band, which is ascribed to Fabry-Perot-type resonances along the wire, as previously reported [42]. SEM images show that the lateral walls of Ga_2O_3 wires are very smooth, resulting in very low surface-scattering losses [42], hence, the most relevant losses are due to the low reflectivity of the wire ends, which can be straightforwardly calculated: $R = 0.096$ for the Ga_2O_3/air boundary supposing normal incidence and a refractive index of Ga_2O_3 of 1.9. This low value, around 10%, explains the low resonance quality. μ-PL spectra from cavities 1 and 2 are also shown in Fig. 3(a), presenting a strong enhancement of modulations, which are ascribed to cavity resonances. Furthermore, main peak wavelength selectivity is shown, cavity 1 presents its maximum at around 690 nm, while in cavity 2 the maximum is at around 715 nm. Besides, a strong polarization dependence of the acquired luminescence is observed. μ-PL polarized spectra from cavities 1 and 2 are shown in Figs. 3(b) and 3(c). The blue solid line shows the spectrum with perpendicular polarization (i.e., the polarizer transmission axis along x, see Fig. 2) while the red solid line shows the spectrum with parallel polarization (i.e., the polarizer transmission axis parallel to z). It is worth mentioning that resonances can be seen along the whole emission band (650–850 nm), a very broad modulation range [50,51], allowing quite a wide wavelength selection in the red-NIR region, as demonstrated in Fig. 3(a). A detailed analysis shows that the main peaks show different positions for each polarization, which is highlighted by the dashed vertical lines. Besides, a complex peak structure is observed due to less intense peaks. In particular, weaker peaks between 695 and 720 nm in Figs. 3(b) and 3(c) perpendicular polarization are highlighted with green dotted lines. The lateral dimensions of the wire make it a multimode fiber for the frequencies corresponding to the studied luminescence band.

Reflectivity of the DBRs is calculated from the finesse value of the resonances within the cavity assuming that the reflectivity is the same for the two DBRs that form the cavity. Finesse values corresponding to the wavelength of

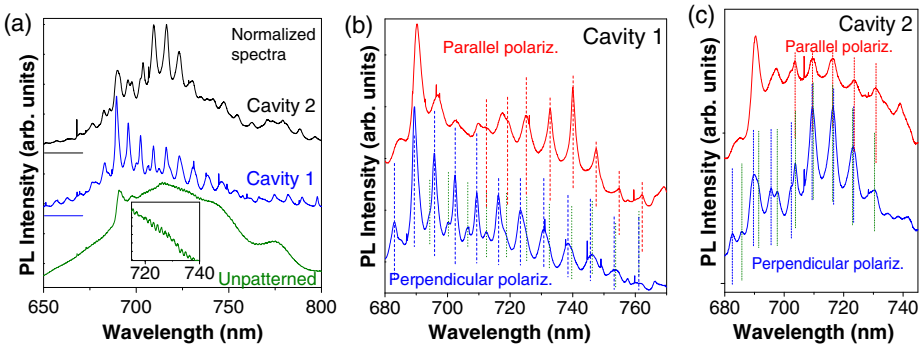

FIG. 3. (a) μ-PL spectra from unpatterned microwire and cavities 1 and 2, perpendicular polarization. Spectra are vertically shifted for the sake of clarity and the base lines are shown. The inset shows a detail of the resonances that could be observed in the unpatterned microwire. (b) μ-PL spectra from cavity 1 acquired with parallel (red, upper spectrum) and perpendicular (blue, lower spectrum) polarizations. (c) Spectra from cavity 2, similar to those shown in (b). Vertical lines show calculated peak positions, as detailed further in the text, for E^x_{11} (dashed blue, lower spectrum), E^x_{12} (dot green, lower spectrum), and E^y_{11} (dashed red, upper spectrum) modes from the obtained L_{eff}, as shown in Fig. 4. All spectra are acquired at room temperature and are normalized.

each peak can be obtained from the ratio of the full width at half maximum of one peak $\Delta\nu_{\mathrm{FWHM}}$ and the free spectral range between this peak and the next one $\delta\nu_{\mathrm{FSR}}$. From these values, reflectivity (R) and finesse (F) can be related by $F = [\pi\sqrt{R}/(1-R)]$ [52]. As shown in Table I, for cavity 1 in perpendicular polarization, $F = 5.1$ for the 709-nm peak and $F = 7.5$ for the peak at 798 nm, resulting in 55% and 66% reflectivity, respectively. For parallel polarization, $F = 4.8$ and $R = 53\%$ for the 740-nm peak. These values are notably higher than reflectivity in the unpatterned wire and comparable to those demonstrated in previous reports on nanowires combined with DBR structures [13,53]. It is to be noticed that values of finesse are also shown for peaks above 800 nm in Table I (see Fig. S1 in the Supplemental Material for a spectrum with these peaks [54]). Finesse cannot be calculated so straightforwardly for most of the peaks from cavity 2, due to broadening caused by the nearness of peaks corresponding to different modes, as seen in Fig. 3(c). The finesse value for the peaks around 700 nm is 3.0 (see Fig. S2 in the Supplemental Material [54]), which means a reflectivity of 37%, i.e., 10%–15% lower than the values obtained for cavity 1 peaks in that range.

Furthermore, the value of the losses at the end facets, which tends to be dominant in micro- and nanocavities due to the small cavity length and small reflection coefficient, can be calculated by the expression $\alpha_m = (1/L)\ln(1/R)$ [55], where L is the effective length of the cavity. For cavity 1, this value is $\alpha_m = 240\ \mathrm{cm}^{-1}$ for the 798-nm peak in perpendicular polarization and $\alpha_m = 370\ \mathrm{cm}^{-1}$ for the 740-nm peak in parallel polarization.

Modal characteristics are of great interest for future applications of potential devices based on this type of cavity. Modes are considered taking into account the wire transversal geometry and the peaks observed in the two different polarizations of the two cavities [Figs. 3(b) and 3(c)]. A sketch of the cross section of the wire is shown in Fig. 1(e). In order to analyze the propagating modes, in a first approximation, it can be regarded as approximately rectangular,

TABLE I. Finesse and reflectivity values obtained for several peaks and polarizations from cavity 1, whose spectra are shown in Figs. 3(a), 3(b), and S1 in the Supplemental Material [54].

Polarization	λ_{peak} [nm]	Finesse	Reflectivity
Perpendicular	696	4.0	0.46
	702	4.8	0.52
	709	5.1	0.55
	716	4.0	0.47
	798	7.5	0.66
	816	6.7	0.63
	826	8.0	0.68
Parallel	725	2.7	0.33
	732	4.3	0.49
	740	4.8	0.53
	747	5.1	0.54

with $a = 2b$. A discussion about the validity of this approximation will be done below. The modes propagating in dielectric waveguides with a rectangular shape are analyzed following the Marcatili [56,57] and Goell [58] models. Marcatili's model presents the advantage of yielding an analytical, closed form for the propagation modes, named E^x_{pq} and E^y_{pq}. The former has $H_x = 0$, while E_x and H_y dominate, and can be considered essentially x polarized. On the other hand, the E^y_{pq} mode has $H_y = 0$ and is essentially y polarized. E^x_{11} and E^y_{11} are the fundamental modes for this geometry. The main peak intensity is expected to occur for these fundamental modes [59]. Polarization of the scattered, detected light is expected to be essentially the same as that of the modes within the wire [60]. Therefore, spectra acquired with perpendicular polarization, E_x components, essentially show resonances resulting from E^x_{11} and, with lower intensity, E^x_{12} propagation modes. On the other hand, parallel polarization detects E_z components, which will be nonzero for E^x_{11}- and E^y_{11}-mode resonances. Besides, the dispersion relation $\omega(k_z)$ can be easily calculated. Indeed, Marcatili's model allows the calculation of k_x, k_y, and k_z for an E^x_{pq} mode at a vacuum wave number k_0 in a rectangular waveguide with transversal dimensions a and b, refractive index n, surrounded by air, according to

$$
\begin{aligned}
k_x \tfrac{a}{2} &= (p-1)\tfrac{\pi}{2} + \arctan\left(\frac{n^2\sqrt{k_0^2(n^2-1)-k_x^2}}{k_x}\right),\\
k_y \tfrac{b}{2} &= (q-1)\tfrac{\pi}{2} + \arctan\left(\frac{\sqrt{k_0^2(n^2-1)-k_y^2}}{k_y}\right),\\
k_z^2 &= k_0^2 n^2 - k_x^2 - k_y^2.
\end{aligned}
\tag{1}
$$

From this equation, k_x and k_y are calculated numerically and, from them, k_z is obtained [57]. However, Marcatili's model is based on two approximations: (i) the mode waves are incident with grazing angles to the lateral waveguide surfaces and (ii) the refractive indices do not differ by more than 50% [57], which is not valid in our work. On the other hand, Goell's model is valid for the general case. It uses the same mode nomenclature, but analyzes them computationally using circular harmonics and does not assume the grazing angle or low refractive-index contrast approximations [58]. In our work, Marcatili's results for E^x_{11} and E^x_{12} modes are virtually equal to those by Goell. However, for E^y_{11} modes, Marcatili's approach does not fit so well and the Goell model is used. Therefore, we calculate k_x, k_y, and k_z values from Eq. (1) for each resonance peak of the perpendicularly polarized spectra, E^x_{11} and E^x_{12} modes, in Figs. 3(b) and 3(c). On the other hand, for the E^y_{11} mode [parallel polarization spectra in Figs. 3(b) and 3(c)] k_z values obtained from Eq. (1) need to be corrected from Marcatili's to Goell's model, which we have done from plots shown in Ref. [45] taking into account that $a \simeq 2b$. Finally, the obtained k_z values for each peak are fitted

according to the longitudinal resonance condition along the optical cavity axis:

$$k_z = l\frac{\pi}{L_{\text{eff}}}, \tag{2}$$

with l being an integer number and L_{eff} the effective length of the cavity. The k_x, k_y, and k_z values for E^x_{11}, E^x_{12}, and E^y_{11} modes for cavities 1 and 2 are displayed in Table S3 in the Supplemental Material [54]. The obtained k_z values are used to get the magnitude of L_{eff} for each mode, imposing Eq. (2) to all the peaks, so that l are consecutive integers for consecutive peaks. Excellent fits are obtained for the different sets of peaks when assigned to these modes. Trials of fitting a set of peaks to a different mode imposing a constant L_{eff} result in sensitively worse fits than the obtained ones.

It should be noted that, although parallel polarization detects E_z components, which will be nonzero for E^x_{11}-, E^x_{12}-, and E^y_{11}-mode resonances, the periodicities observed in Fig. 3 between some peaks around 740 nm for parallel polarization agree better with the E^y_{11} modes than with the E^x_{11} ones. Besides, if they were E^x_{11} or E^x_{12}, they would be observed for both polarizations. Therefore, resonances for parallel polarization are assigned to the E^y_{11} mode.

Figure 4 shows the dispersion relations for the sets of peaks corresponding to E^x_{11}, E^x_{12}, and E^y_{11} modes, as obtained by Marcatili's model for the first two modes and by Goell's model for the E^y_{11} mode. Figure 4(a) shows the results for cavity 1. The obtained effective length value that fulfills the resonance condition is $L_{\text{eff},11} = 17.4$ μm for all modes. This L_{eff} value is notably longer than $L_1 = 15.2$ μm of cavity 1. This is explained because an effective penetration depth, i.e., an effective shift of the interface into the mirror, must be taken into account in a DBR. For an ideal, planar, infinite DBR it is given by the expression

$$\delta_{\text{eff}} = \frac{\bar{n}\lambda_B}{4n\Delta n} + \frac{\lambda_B \Delta n}{2\pi^2 n\bar{n}}, \tag{3}$$

with $\bar{n}$ being the average refractive index, $\lambda_B = 2\bar{n}\Lambda$ the Bragg wavelength, Λ the DBR period, n the Ga_2O_3 refractive index, and Δn the refractive-index contrast [61]. We obtain a penetration depth value of $\delta_{\text{eff}} = 900$ nm, but we remark that this is a rough estimation. This value should be taken into account in the two DBRs and, therefore, the effective confinement length would be estimated this way as $L_{\text{eff,calc}} = L_1 + 2\delta_{\text{eff}} = 17$ μm. This is comparable to the value $L_{\text{eff},11} = 17.4$ μm of this optical cavity. Figure 4(b) shows analogous dispersion relations for cavity 2. The obtained values for cavity 2, $L_{\text{eff},11} = 17.2$ μm for E^x_{11} and E^y_{11} and $L_{\text{eff},12} = 17.1$ μm for E^x_{12}, agree with the expected values, as $L_2 = 15.0$ μm, as measured on the SEM, i.e., 0.2-μm shorter than cavity 1.

In order to achieve a more complete assessment of the behavior of these DBR cavities, FDTD simulations are

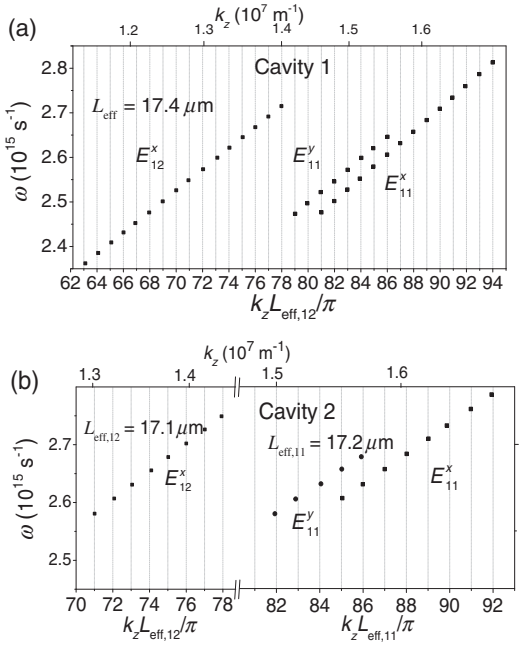

FIG. 4. (a) Dispersion relations obtained from the luminescence peak positions in cavity 1 for E^x_{11}, E^x_{12} (perpendicular polarization spectrum), and E^y_{11} modes (parallel polarization spectrum) from Fig. 3(b). The Marcatili approximation is used for E^x_{11} and E^x_{12} modes and Goell calculations for the E^y_{11} mode. Effective length L_{eff} values are calculated imposing k_z to be proportional to consecutive integer numbers l for consecutive resonance peaks. (b) E^x_{11}, E^y_{11}, and E^x_{12} modes in cavity 2 from Fig. 3(c), using the same procedure. In both cases, k_z values shown in the upper axis correspond to those from Marcatili's model.

carried out using the commercial OptiFDTD software to evaluate the Poynting vector amplitude within the wire and the reflected power spectra of our DBR cavity. The experimentally determined dimensions and actual cross section of the wire, as well as those of the fabricated DBRs [see Figs. 1(b) and 1(e)] are implemented for the simulations (see Fig. S4 in the Supplemental Material [54]). Marcatili's model provides the field components and Poynting vector module for the fundamental E^x_{11} mode within a rectangular waveguide (see Eq. S5 in Supplemental Material [54]). Figure 5(a) represents the Poynting vector amplitude as obtained from Marcatili's model for the fundamental, E^x_{11} propagating mode at 709-nm vacuum wavelength. A comparison of the actual cross-section shape (orange dashed line) and the rectangular approximation (white dashed line) used for Marcatili's approximation is also provided in this figure. Figure 5(b) represents the intensity obtained with the FDTD simulations for the fundamental mode of a wave with 709-nm vacuum wavelength, propagating along the waveguide. Excellent agreement is obtained between these two figures. In both cases, the Poynting vector tends to be negligible in the waveguide boundaries, especially in the rectangle's corners, as supposed in Marcatili's model. This

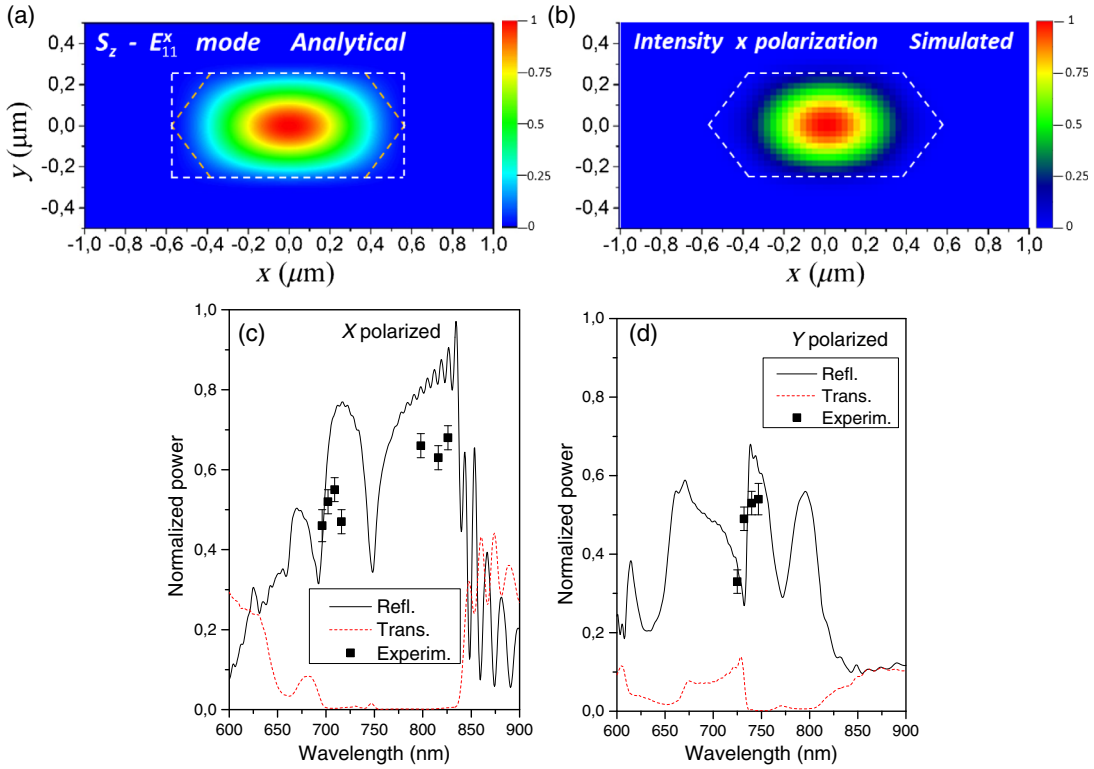

FIG. 5. Comparison between Poynting vector value along the waveguide cross section for (a) the Marcatili E_{11}^x mode at 709 nm, calculated analytically, and (b) the FDTD-simulated 709 nm x-polarized wave. Dashed white lines show the waveguide-air interface in each model. Dashed orange lines in (a) indicate the real interface, for the sake of comparison. (c) The simulated FDTD reflected power spectrum on one DBR of cavity 1 for x polarization and (d) y polarization. Black squares show R values obtained from finesse calculations (Table I).

explains the fact that this approximation works very well to fit the analytical dispersion relations (Fig. 4) and the experimental PL resonances [Figs. 3(b) and 3(c)].

Reflectivity as a function of the frequency within the studied range is obtained via FDTD simulations. A linearly polarized short pulse is generated to propagate towards the DBR, and the reflected signal is detected. The frequency dependence of the reflected power is analyzed by Fourier transform of the detected Poynting vector, as shown in Figs. 5(c) and 5(d), black lines, for x polarization and y polarization in cavity 1, respectively. As discussed above, x polarization essentially corresponds to E_{pq}^x modes, while y polarization essentially corresponds to E_{pq}^y modes. Reflectivities up to about 90% are obtained with the simulations in the represented range, similar to other systems based on patterned DBRs on wires [13].

For x polarization, within the experimental spectral range (650–800 nm) two maxima are obtained, one around 715 nm and the other one in 800 nm. A local minimum of reflectivity is found between these two maxima, around 750 nm. On the other hand, for y polarization a maximum at 740 nm is found, with two minima at around 732 and 772 nm. These features agree very well with finesse values of peaks observed for x and y polarizations in cavity 1 [see Fig. 3(b)]. It is observed, for both experimental values and simulation results, that, in general, reflectivity is higher for x polarization than for y polarization.

The obtained reflectivity spectra for cavity 1 are compared with several values calculated from experimental finesse [see Table I]. These are indicated with black squares in Figs. 5(c) and 5(d). A good agreement is obtained between simulation and experimental values, except that experimental values are systematically lower than simulated ones. This fact is expected due to the experimental dispersion of the real values of α and γ in the DBRs. A clear difference is observed for the reflectivity minimum around 750 nm for x polarization, which is quite broader when calculated from the experimental finesse than from the simulation.

Simulated transmission spectra are also shown, solid red lines in Figs. 5(c) and 5(d). The stop band for x polarization covers essentially the whole emission band of Cr^{3+} in Ga_2O_3, as desired. For y polarization, the stop band is not so efficient and covers a narrower range, from about 740 to about 800 nm.

It is worth mentioning that higher reflectivity values can be obtained in future works with this fabrication method by further optimizing the DBRs, reaching a better light confinement within the cavities by, e.g., reduction of radiation losses by optimizing the DBR design in order to get a good impedance mismatch [9].

IV. CONCLUSIONS

Strongly modulated, room-temperature red-IR luminescence is achieved within optical cavities fabricated within chromium-doped gallium-oxide microwires behaving as waveguides. FIB drilling is used in order to fabricate DBRs that effectively confine light within the cavity. The peaks with maximum intensity are shown to be different in cavities with different parameters, demonstrating tunability along a wide spectral range of the main emission wavelength. Furthermore, the main luminescence peak position in a single cavity strongly depends on its polarization, as demonstrated by μ-PL spectra. A thorough analysis of the optical modes, both by analytical approximations and FDTD simulations, is carried out to explain the experimental, polarized μ-PL spectra. E^x_{11}, E^x_{12}, and E^y_{11} rectangular waveguide propagating modes result in different resonant peak sets, corresponding to successive longitudinal resonance modes. Dispersion relations are obtained, which allow a calculation of the effective cavity length, around 2 -μm longer than the actual cavity length, which is explained by the DBR penetration depths. Reflectivity values of the DBRs obtained from the experimental finesse values of the resonances are compared with the reflectivity spectrum calculated via FDTD simulations, showing a good agreement in the positions of the maxima. Maximum experimental reflectivity values are between 50% and 70% in the studied range, and simulations demonstrate that reflectivities up to about 90% could be reached, paving the way for the design of high reflectivity and tunability of DBR optical devices.

ACKNOWLEDGMENTS

This work has been supported by MINECO (Projects No. MAT 2015-65274-R-FEDER, No. MAT2016-81720-REDC). M. A.-O. acknowledges financial support from MECD (FPU Contract No. FPU15/01982). The authors would like to thank Steven A. Hindmarsh and Ana M. Sánchez from the University of Warwick for the first trials with FIB milling.

[1] M. T. Hill and M. C. Gather, Advances in small lasers, Nat. Photonics **8**, 908 (2014).

[2] S. Yang, Y. Wang, and H. Sun, Advances and prospects for whispering gallery mode microcavities, Adv. Opt. Mater. **3**, 1136 (2015).

[3] D. Venkatakrishnarao, M. A. Mohiddon, and R. Chandrasekar, The photonic side of curcumin: Microsphere resonators self-assembled from curcumin derivatives emitting visible/near-infrared light, Adv. Opt. Mater. **5**, 1600613 (2017).

[4] Y. Liu, H. Dong, J. Lu, J. Zhan, J. Li, Z. Chen, and L. Zhang, Free-standing, single-crystalline parallelogram Sb shallow-doped ZnO wave-guided optical resonators, Adv. Opt. Mater. **2**, 1090 (2014).

[5] Q. Guo, H. Zhu, F. Liu, A. Y. Zhu, J. C. Reed, F. Yi, and E. Cubukcu, Silicon-on-glass graphene-functionalized leaky cavity mode nanophotonic biosensor, ACS Photonics **1**, 221 (2014).

[6] T. Zhong, J. M. Kindem, J. G. Bartholomew, J. Rochman, I. Craiciu, E. Miyazono, M. Bettinelli, E. Cavalli, V. Verma, S. W. Nam, F. Marsili, M. D. Shaw, A. D. Beyer, and A. Faraon, Nanophotonic rare-earth quantum memory with optically controlled retrieval, Science **357**, 1392 (2017).

[7] Q. Liu, P. Romero-Gomez, P. Mantilla-Perez, S. Colodrero, J. Toudert, and J. A. Martorell, Two-resonance tapping cavity for an optimal light trapping in thin-film solar cells, Adv. Energy Mater. **7**, 1700356 (2017).

[8] J. S. Foresi, P. R. Villeneuve, J. Ferrera, E. R. Thoen, G. Steinmeyer, S. Fan, J. D. Joannopoulos, L. C. Kimerling, H. I. Smith, and E. P. Ippen, Photonic-bandgap microcavities in optical waveguides, Nature (London) **390**, 143 (1997).

[9] D. Peyrade, E. Silberstein, P. Lalanne, A. Talneau, and Y. Chen, Short Bragg mirrors with adiabatic modal conversion, Appl. Phys. Lett. **81**, 829 (2002).

[10] C. J. Barrelet, J. Bao, M. Loncar, H.-G. Park, F. Capasso, and C. M. Lieber, Hybrid single-nanowire photonic crystal and microresonator structures, Nano Lett. **6**, 11 (2006).

[11] G. Crosnier, D. Sanchez, S. Bouchoule, P. Monnier, G. Beaudoin, I. Sagnes, R. Raj, and F. Raineri, Hybrid indium phosphide-on-silicon nanolaser diode, Nat. Photonics **11**, 297 (2017).

[12] Y. Liu, C. Meng, A. P Zhang, Y. Xiao, H. Yu, and L. Tong, Compact microfiber Bragg gratings with high-index contrast, Opt. Lett. **36**, 3115 (2011).

[13] A. Fu, H. Gao, P. Petrov, and P. Yang, Widely tunable distributed bragg reflectors integrated into nanowire waveguides, Nano Lett. **15**, 6909 (2015).

[14] L. Chen and E. Towe, Nanowire lasers with distributed-Bragg-reflector mirrors, Appl. Phys. Lett. **89**, 053125 (2006).

[15] L. Wei, A. Khattak, C. Martz, and D.-P. Zhou, Tunable multimode fiber based filter and its application in cost-effective interrogation of fiber-optic temperature sensors, IEEE Photonics J. **9**, 7101808 (2017).

[16] L. G. Wright, D. N. Christodoulides, and F. W. Wise, Controllable spatiotemporal nonlinear effects in multimode fibres, Nat. Photonics **9**, 306 (2015).

[17] M. Kracht, A. Karg, J. Schörmann, M. Weinhold, D. Zink, F. Michel, M. Rohnke, M. Schowalter, B. Gerken, A. Rosenauer, P. J. Klar, J. Janek, and M. Eickhoff, Tin-Assisted Synthesis of ε-Ga_2O_3 by Molecular Beam Epitaxy, Phys. Rev. Applied **8**, 054002 (2017).

[18] E. G. Villora, K. Shimamura, Y. Yoshikawa, T. Ujiie, and K. Aoki, Electrical conductivity and lattice expansion of β-Ga_2O_3 below room temperature, Appl. Phys. Lett. **92**, 202120 (2008).

[19] M. Higashiwaki, K. Sasaki, T. Kamimura, M. H. Wong, D. Krishnamurthy, A. Kuramata, T. Masui, and S. Yamakoshi, Depletion-mode Ga_2O_3 metal-oxide-semiconductor field-effect transistors on β-Ga_2O_3 (010) substrates and temperature dependence of their device characteristics, Appl. Phys. Lett. **103**, 123511 (2013).

[20] A. J. Green, K. D. Chabak, M. Baldini, N. Moser, R. Gilbert, R. C. Fitch Jr., G. Wagner, Z. Galazka, J. McCandless, A.

Crespo, K. Leedy, and G. H. Jessen, β-Ga_2O_3 MOSFETs for radio frequency operation, IEEE Electron Device Lett. **38**, 790 (2017).

[21] D. Yan, G. Yin, Z. Huang, X. Liao, Y. Kang, Y. Yao, B. Hao, J. Gu, and D. Han, Biomineralization of uniform gallium oxide rods with cellular compatibility, Inorg. Chem. **48**, 6471 (2009).

[22] X.-S. Wang, W.-S. Li, J.-Q. Situ, X.-Y. Ying, H. Chen, Y. Jin, and Y.-Z. Du, Multi-functional mesoporous β-$Ga_2O_3:Cr^{3+}$ nanorod with long lasting near infrared luminescence for *in vivo* imaging and drug delivery, RSC Adv. **5**, 12886 (2015).

[23] M. Zapf, R. Röder, K. Winkler, L. Kaden, J. Greil, M. Wille, and C. Ronning, Dynamical tuning of nanowire lasing spectra, Nano Lett. **17**, 6637 (2017).

[24] B. Henderson and G. F. Imbusch, *Optical Spectroscopy of Inorganic Solids* (Clarendon, Oxford, U.K., 1989), Chap. 5.

[25] X. Liu, Q. Zhang, Q. Xiong, and T. C. Sum, Tailoring the lasing modes in semiconductor nanowire cavities using intrinsic self-absorption, Nano Lett. **13**, 1080 (2013).

[26] E. Nogales, J. A. Garcia, B. Mendez, and J. Piqueras, Red luminescence of Cr in β-Ga_2O_3 nanowires, J. Appl. Phys. **101**, 033517 (2007).

[27] E. Nogales, I. Lopez, B. Mendez, J. Piqueras, K. Lorenz, E. Alves, and J. A. Garcia, Doped gallium oxide nanowires for photonics, Proc. SPIE Int. Soc. Opt. Eng. **8263**, 82630B (2012).

[28] G. Pozina, M. Forsberg, M. A. Kaliteevski, and C. Hemmingsson, Emission properties of Ga_2O_3 nano-flakes: Effect of excitation density, Sci. Rep. **7**, 42132 (2017).

[29] S. C. Vanithakumari and K. K. Nanda, A one step method for the growth of Ga_2O_3 nanorod based white light emitting phosphors, Adv. Mater. **21**, 3581 (2009).

[30] T. Miyata, T. Nakatani, and T. Minami, Gallium oxide as host material for multicolor emiting phosphors, J. Lumin. **87–89**, 1183 (2000).

[31] J. Hao, Z. Lou, I. Renaud, and M. Cocivera, Electroluminescence of europium-doped gallium oxide thin films, Thin Solid Films **467**, 182 (2004).

[32] Z. Chen, X. Wang, F. Zhang, S. Noda, K. Saito, T. Tanaka, M. Nishio, M. Arita, and Q. Guo, Observation of low voltage driven green emission from erbium doped Ga_2O_3 light-emitting devices, Appl. Phys. Lett. **109**, 022107 (2016).

[33] M. Higashiwaki and G. H. Jessen, The dawn of gallium oxide microelectronics, Appl. Phys. Lett. **112**, 060401 (2018).

[34] S. J. Pearton, J. Yang, P. H. Cary IV, F. Ren, J. Kim, M. J. Tadjer, and M. A. Mastro, A review of Ga_2O_3 materials, processing and devices, Appl. Phys. Rev. **5**, 011301 (2018).

[35] M. Law, D. J. Sirbuly, J. C. Johnson, J. Goldberger, R. J. Saykally, and P. Yang, Nanoribbon waveguides for subwavelength photonics integration, Science **305**, 1269 (2004).

[36] H. Ota and H. Hosono, Transparent oxide optoelectronics, Mater. Today **7**, 42 (2004).

[37] Y. Li, T. Tokizono, M. Liao, M. Zhong, Y. Koide, I. Yamada, and J.-J. Delaunay, Efficient assembly of bridged β-Ga_2O_3 nanowires for solar-blind photodetection, Adv. Funct. Mater. **20**, 3972 (2010).

[38] P. Gutruf, E. Zeller, S. Walia, H. Nili, S. Sriram, and M. Bhaskaran, Stretchable and tunable microtectonic ZnO-based sensors and photonics, Small **11**, 4532 (2015).

[39] S. Yamaoka, Y. Furukawa, and M. Nakayama, Initial process of photoluminescence dynamics of self-trapped excitons in a β-Ga_2O_3 single crystal, Phys. Rev. B **95**, 094304 (2017).

[40] K. Shimamura, E. G. Villora, T. Ujiie, and K. Aoki, Excitation and photoluminescence of pure and Si-doped β-Ga_2O_3 single crystals, Appl. Phys. Lett. **92**, 201914 (2008).

[41] E. Nogales, J. A. Garcia, B. Mendez, and J. Piqueras, Doped gallium oxide nanowires with waveguiding behavior, Appl. Phys. Lett. **91**, 133108 (2007).

[42] I. Lopez, E. Nogales, B. Mendez, and J. Piqueras, Resonant cavity modes in gallium oxide microwires, Appl. Phys. Lett. **100**, 261910 (2012).

[43] G. Martinez-Criado, J. Segura-Ruiz, M. H. Chu, R. Tucoulou, I. Lopez, E. Nogales, B. Mendez, and J. Piqueras, Crossed Ga_2O_3/SnO_2 multiwire architecture: A local structure study with nanometer resolution, Nano Lett. **14**, 5479 (2014).

[44] M. Alonso-Orts, A. M Sanchez, S. A Hindmarsh, I. Lopez, E. Nogales, J. Piqueras, and B. Mendez, Shape engineering driven by selective growth of SnO_2 on doped Ga_2O_3 nanowires, Nano Lett. **17**, 515 (2017).

[45] I. Lopez, E. Nogales, B. Mendez, J. Piqueras, A. Peche, J. Ramirez-Castellanos, and J. M. Gonzalez-Calbet, Influence of Sn and Cr doping on morphology and luminescence of thermally grown Ga_2O_3 nanowires, J. Phys. Chem. C **117**, 3036 (2013).

[46] Y. Tokida and S. Adachi, Photoluminescence spectroscopy and energy-level analysis of metal-organic-deposited $Ga_2O_3:Cr^{3+}$ films, J. Appl. Phys. **112**, 063522 (2012).

[47] J. F. Gomez-Cortes, M. L. No, I. Lopez-Ferreño, J. Hernandez-Saz, S. I Molina, A. Chuvilin, and J. M. San Juan, Size effect and scaling power-law for superelasticity in shape-memory alloys at the nanoscale, Nat. Nanotechnol. **12**, 790 (2017).

[48] M. F. Al-Kuhaili, S. M. A Durrani, and E. E. Khawaja, Optical properties of gallium oxide films deposited by electron-beam evaporation, Appl. Phys. Lett. **83**, 4533 (2003).

[49] R.-M. Ma, X.-L. Wei, L. Dai, S.-F. Liu, T. Chen, S. Yue, Z. Li, Q. Chen, and G. G. Qin, Light coupling and modulation in coupled nanowire ring–Fabry-Pérot cavity, Nano Lett. **9**, 2697 (2009).

[50] S. Riechel, U. Lemmer, J. Feldmann, S. Berleb, A. G. Mückl, W. Brütting, A. Gombert, and V. Wittwer, Very compact tunable solid-state laser utilizing a thin-film organic semiconductor, Opt. Lett. **26**, 593 (2001).

[51] B. Xue, B. Fan, M. Cathelinaud, X. Fan, and X. Zhang, Towards ultra-broad emission band by luminescent film with continuously tunable emission wavelength, Opt. Mater. Express **4**, 1159 (2014).

[52] M. Suter and P. Dietiker, Calculation of the finesse of an ideal Fabry-Perot resonator, Appl. Opt. **53**, 7004 (2014).

[53] J. Kong, S. Chu, J. Huang, M. Olmedo, W. Zhou, L. Zhang, Z. Chen, and J. Liu, Use of distributed Bragg reflectors to

enhance Fabry-Pérot lasing in vertically aligned ZnO nanowires, Appl. Phys. A **110**, 23 (2013).

[54] See Supplemental Material at http://link.aps.org/supplemental/10.1103/PhysRevApplied.9.064004 for the normalized μ-PL spectra from cavity 1 in the IR range and the finesse calculation in the 700-nm range for cavity 2, for the tables with k_x, k_y, k_z, and l values obtained for the different peaks and modes for both cavities, for the layout of the simulated DBR for cavity 1, and for the equations of the field components and Poynting vector modulus within a rectangular waveguide for the fundamental E_{x11} mode within Marcatili's model.

[55] M. A. Zimmler, F. Capasso, S. Müller, and C. Ronning, Optically pumped nanowire lasers: Invited review, Semicond. Sci. Technol. **25**, 024001 (2010).

[56] K. Okamoto, *Fundamentals of Optical Waveguides*, 2nd ed. (Elsevier Academic Press, London, U.K., 2005), p. 27.

[57] E. A. Marcatili, Dielectric rectangular waveguide and directional coupler for integrated optics, J. Bell Syst. Tech. J. **48**, 2071 (1969).

[58] J. E. Goell, in *Introduction to Integrated Optics*, edited by M. Barnoski (Plenum Press, New York, 1974), p. 79.

[59] W. D. Laakmann and W. H. Steier, Waveguides: Characteristic modes of hollow rectangular dielectric waveguides, Appl. Opt. **15**, 1334 (1976).

[60] D. Saxena, F. Wang, Q. Gao, S. Mokkapati, H. H. Tan, and C. Jagadish, Mode profiling of semiconductor nanowire lasers, Nano Lett. **15**, 5342 (2015).

[61] L. R. Brovelli and U. Keller, Simple analytical expressions for the reflectivity and the penetration depth of a Bragg mirror between arbitrary media, Opt. Commun. **116**, 343 (1995).

Correction: A conversion error in Eq. (1) has been fixed.